Overturning Circulation Pathways in a Two-Basin Ocean Model®

LOUIS-PHILIPPE NADEAU

Institut des Sciences de la Mer de Rimouski, Université du Québec à Rimouski, Rimouski, Quebec, Canada

MALTE F. JANSEN

Department of the Geophysical Sciences, University of Chicago, Chicago, Illinois

(Manuscript received 4 February 2020, in final form 15 May 2020)

ABSTRACT

A toy model for the deep ocean overturning circulation in multiple basins is presented and applied to study the role of buoyancy forcing and basin geometry in the ocean's global overturning. The model reproduces the results from idealized general circulation model simulations and provides theoretical insights into the mechanisms that govern the structure of the overturning circulation. The results highlight the importance of the diabatic component of the meridional overturning circulation (MOC) for the depth of North Atlantic Deep Water (NADW) and for the interbasin exchange of deep ocean water masses. This diabatic component, which extends the upper cell in the Atlantic below the depth of adiabatic upwelling in the Southern Ocean, is shown to be sensitive to the global area-integrated diapycnal mixing rate and the density contrast between NADW and Antarctic Bottom Water (AABW). The model also shows that the zonally averaged global overturning circulation is to zeroth-order independent of whether the ocean consists of one or multiple connected basins, but depends on the total length of the southern reentrant channel region (representing the Southern Ocean) and the global ocean area integrated diapycnal mixing. Common biases in single-basin simulations can thus be understood as a direct result of the reduced domain size.

1. Introduction

By controlling the oceanic uptake and abyssal storage of atmospheric heat and carbon, the global ocean meridional overturning circulation (MOC) plays a central role in Earth's climate. Changes in circulation and stratification affect the ventilation rate of the deep ocean and may have played a key role in explaining the observed swings in atmospheric carbon dioxide concentration between glacial and interglacial periods (e.g., Brovkin et al. 2007; Adkins 2013; Watson et al. 2015; Marzocchi and Jansen 2019). Proxy data of the Last Glacial Maximum (LGM) suggest that the volume occupied by the lower cell of the MOC expanded significantly

Supplemental information related to this paper is available at the Journals Online website: https://doi.org/10.1175/JPO-D-20-0034.s1.

Both authors contributed equally to this work.

Corresponding author: Louis-Philippe Nadeau, louis-philippe_nadeau@ugar.ca

compared to its present day value (Curry and Oppo 2005). This, combined with potential changes in air–sea gas exchange due to increased sea ice cover (Stephens and Keeling 2000) or modulations in the efficiency of the surface biological productivity (Sigman and Boyle 2000) likely led to the observed draw down in atmospheric CO₂ during the LGM. Yet, the oceanic storage of atmospheric tracers critically depends on how tracers are distributed in each ocean basin, which is in turn controlled by the three-dimensional trajectory of the circulation in the global ocean. Despite recent theoretical advances on how the zonally averaged global circulation responds to external forcing, many open questions remain on how the MOC connects between the ocean basins through the circumpolar channel. Here, we aim to improve our understanding of this multibasin circulation and its relationship to theories that have been developed in the single-basin context.

To illustrate what is meant by interbasin exchange and how this impacts the abyssal ventilation rate, we show in Fig. 1 the main possible pathways (or circulation "modes") of a simplified two-basin ocean, where the bottom two circulation patterns can be thought of as arising from

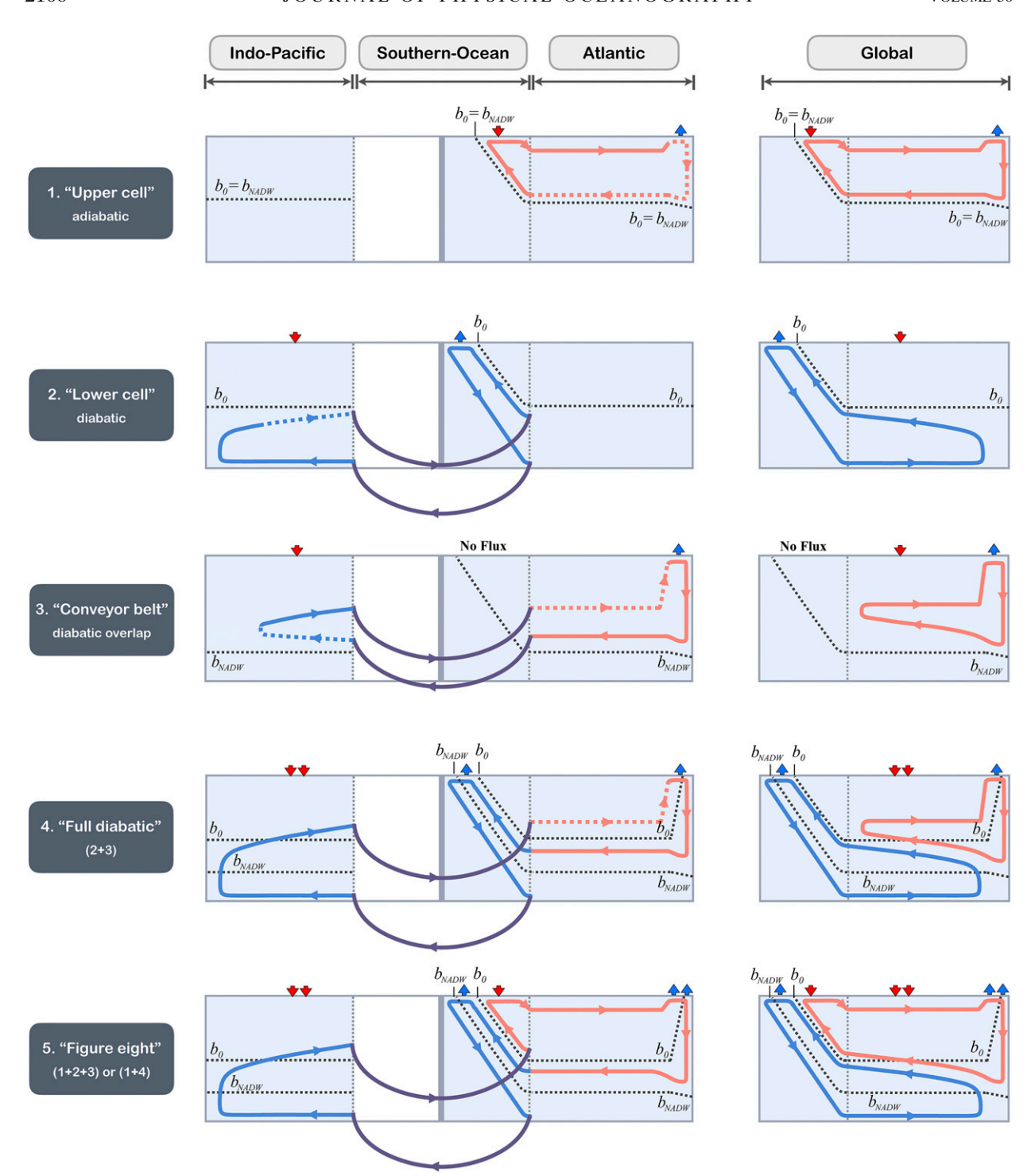


FIG. 1. Possible overturning pathways in a two-basin ocean: 1) adiabatic upper cell, 2) diabatic lower cell, 3) conveyor belt, 4) full diabatic overturning, and 5) figure eight. (left) Sketches of the streamfunction separated into the Indo-Pacific and Atlantic basins, where the Indo-Pacific has been mirrored to illustrate the connection via the Southern Ocean (i.e., north is to the right in the Atlantic but to the left in the Indo-Pacific). (right) The resulting global mean overturning streamfunction. Notice that the pathways in 4 and 5 can be constructed from a superposition of the circulation modes 1, 2, and 3. The dotted red lines in 1–3 and the dotted blue lines in 2 and 3 cancel each other in the superposition. The blue and red arrows at the surface indicate a negative and positive surface buoyancy flux, respectively. The circulations in the Atlantic interior and in the Southern Ocean are assumed to be adiabatic in this simplified schematic.

2107

superpositions of the first three modes [which in turn are similar to the pathways discussed by Ferrari et al. (2017)]. The left panels show a latitude-depth schematic of the MOC spanning the Indo-Pacific, the Southern Ocean (SO), and the Atlantic. The corresponding globally integrated circulation is shown in the right panels. To simplify the discussion, we focus on a unique zonally symmetric channel sector connected to two basins to the north. We also assume that diapycnal processes are limited to the three following regions: the Indo-Pacific, the surface of the Southern Ocean, and the Atlantic deep water production region. The circulation in the interior of the Atlantic basin and in the Southern Ocean are for now assumed to be adiabatic. [Diabatic overturning contributions within these regions may be important in some cases (e.g., Sun et al. 2018) and could be added as additional circulation modes, but are neglected here for simplicity.] Two isopycnal surfaces are key to define the circulation modes: (i) the buoyancy b_0 , which marks the division between positive and negative buoyancy fluxes at the surface of the Southern Ocean-like channel, and (ii) the buoyancy b_{NADW} , which marks the minimum buoyancy of North Atlantic Deep Water (NADW). As we explain below, the interval $b_0 > b > b_{\text{NADW}}$ defines the range of overlapping buoyancies between the Atlantic upper cell and Indo-Pacific lower cell. Any transport in this range implies an interbasin exchange.

The first row of Fig. 1 shows the adiabatic "upper cell" circulation mode (e.g., Toggweiler and Samuels 1998; Wolfe and Cessi 2011), for which there is a pole-to-pole compensation between negative surface buoyancy fluxes in the North Atlantic and positive surface buoyancy fluxes in the Southern Ocean. Water that sinks at buoyancy $b \ge b_{\text{NADW}}$ in the North Atlantic upwells adiabatically at the surface of the channel, north of b_0 . Thus, in this scenario, $b_{NADW} = b_0$ and this adiabatic upper cell exists only in the Atlantic. The second row of Fig. 1 shows the "lower cell" circulation mode (e.g., Nikurashin and Vallis 2011), for which negative surface buoyancy fluxes around Antarctica (blue arrow south of b_0) are compensated by diapycnal mixing and ultimately surface buoyancy loss in the Indo-Pacific (Newsom and Thompson 2018). By definition, no transport overlap can occur between the two first modes, as the upper cell and lower cell only exist above and below b_0 , respectively. In a globally integrated perspective, the superposition of the first two modes corresponds to the standard picture with two distinct cells stacked on top of each other.

The situation, however, gets more involved if we consider a third circulation mode, which resembles the "conveyor belt" of Broecker (1991) (third row of Fig. 1). This circulation mode involves no water mass

transformations at the surface of the channel. Instead NADW in the range $b > b_{\rm NADW}$ flows into the Indo-Pacific via a geostrophic interbasin transport resulting from the isopycnal height difference between the two basins (e.g., Jones and Cessi 2016; Ferrari et al. 2017). Diabatic upwelling in the Indo-Pacific basin then transforms this former NADW into lighter water that flows back to the Atlantic, thus closing the conveyor belt loop. The resulting overturning circulations in the Indo-Pacific and Atlantic in this case are part of a single interbasin overturning cell, where buoyancy loss during deep water formation in the North Atlantic is balanced by diffusive buoyancy gain in the Indo-Pacific. The globally integrated MOC corresponding to this mode yields a single diabatic upper cell (middle-right panel).

The superposition of the diabatic lower cell and conveyor belt modes gives the "full diabatic" circulation, an example of which is shown in the fourth row of Fig. 1. In this scenario, NADW in the range $b_0 > b > b_{NADW}$ upwells adiabatically at the surface of the channel, south of b_0 . Exposed to negative buoyancy fluxes, this former NADW is transformed into denser water that fills the bottom of the Indo-Pacific (e.g., Lumpkin and Speer 2007; Talley 2013). Diapycnal mixing in the Indo-Pacific allows for the upwelling of this water above the isopycnal b_0 before returning back to the North Atlantic (for the specific superposition chosen here, the dotted blue lines in modes 2 and 3 cancel each other to yield a single lower cell in the Indo-Pacific). The globally integrated MOC corresponding to this fourth pathway yields a lower cell in addition to a diabatic upper cell, but unlike in the superposition of modes 1 and 2, the two cells are now directly coupled. In the globally averaged picture this coupling remains evident in the existence of shared buoyancy classes between the upper and lower cell (i.e., the range $b_0 > b > b_{NADW}$).

The bottom row of Fig. 1 shows the "figure eight" circulation, as sketched in Ferrari et al. (2014), which can be viewed as a superposition of all of the first three modes. The figure eight is thus a combination of diabatic and adiabatic pathways. It differs from the full diabatic pathway only by the upper branch of the Atlantic MOC (AMOC), which connects adiabatically to the surface of the channel, where it is exposed to positive buoyancy fluxes north of b_0 . (Notice that the dotted red lines in modes 1 and 3 cancel each other.) The globally integrated MOC again yields two coupled cells with shared isopycnals, and the mixing rate between the two cells is expected to be significantly enhanced.

It is worth noting that the overturning patterns in the last two rows of Fig. 1 describe the overturning from a basin-integrated perspective, which is not necessarily representative of the specific trajectory of an individual

water parcel, which is affected by the zonal structure of the circulation within the basins and the Southern Ocean. In practice, the meandering ACC, horizontal gyres, and mesoscale eddies are likely to cause substantial stirring, which will lead to a divergence of parcel trajectories. Nevertheless, we believe that the distinct overturning pathways in Fig. 1, and in particular the existence or lack of shared isopycnals between the upper and lower overturning cell, play an important role in governing the transport and distribution of tracers in the ocean.

In practice, the various pathways of Fig. 1 coexist to explain the observed MOC. According to the Estimating the Circulation and Climate of the Ocean (ECCO) state estimate, about half of the AMOC at 30°S closes onto itself through the adiabatic upper cell mode (Cessi 2019). The remaining half is coupled to the lower cell through interbasin exchange via a diabatic pathway. In other words, the present-day AMOC can be viewed as a superposition of an adiabatic upper cell and a diabatic extension that loops through the Indo-Pacific either directly or indirectly through water mass transformations at the surface of the Southern Ocean. This diabatic extension is believed to have significantly weakened during the Last Glacial Maximum, leading to a shoaling of the AMOC. There exists a wide consensus that the buoyancy contrast between Antarctic Bottom Water (AABW) and NADW plays a key role in controlling the AMOC's strength and depth (e.g., Jansen and Nadeau 2016; Jansen 2017; Nadeau et al. 2019; Sun et al. 2020; Baker et al. 2020). An objective of this study is to better understand what controls the partitioning between coupled and uncoupled modes of circulation, and how this explains the resulting overturning in each basin as well as its global average.

The conveyor belt mode, which is key to the interbasin exchange, has been the focus of recent studies using different versions of an idealized two layer model (e.g., Jones and Cessi 2016; Cessi and Jones 2017; Ferrari et al. 2017). The model captures the essential characteristics of the direct interbasin exchange and compares well with the results of an OGCM. Yet, such models cannot reproduce the figure eight pathway, which requires at least three layers (i.e., two pycnoclines). Thompson et al. (2016) consider a four-layer model and show that a continuous transition from an uncoupled circulation with two distinct cells to the figure eight pathway can be achieved by decreasing NADW production (assuming a fixed AABW production). However, results are somewhat limited by the externally prescribed NADW production rates and the discrete layer representation, where the buoyancy classes associated with the different water masses are fixed. In practice, a change in NADW

production as a result of reduced surface buoyancy loss would likely also increase the buoyancy of NADW, thus possibly reducing the transport overlap with the lower cell in the Southern Ocean, rather than promoting it.

To circumvent issues related to the discrete nature of the layer representation, Jansen and Nadeau (2019, hereafter JN19) recently developed a multicolumn toy model for the meridional overturning circulation, which uses multiple vertically continuous one-dimensional buoyancy profiles in key regions of the domain. In these regions, the model solves predictive residual advectiondiffusion equations that are coupled to each other using diagnostic relationships for the residual overturning circulation. Using a simplified configuration, JN19 show that the toy model results reproduce those from an OGCM for the transient response to surface warming. While JN19 focus on a simplified one basin configuration, the model will here be adapted to explore the sensitivity of the partitioning between coupled and uncoupled circulation modes in a multibasin setup.

This study is organized around three main objectives. First, in section 2, we extend the model of JN19 to include a second basin, thus allowing for interbasin exchange and overlap between the two cells of the MOC. In section 3, we then investigate the effect of AABW density and diapycnal mixing on the overlap, comparing the results of the toy model with those of a general circulation model (GCM) with an idealized two-basin geometry. We introduce a decomposition of the Atlantic meridional overturning into an adiabatic component (uncoupled mode) and a diabatic component (coupled mode). We illustrate that the coupled mode weakens with the buoyancy contrast between AABW and NADW and strengthens with increased vertical diffusivity. To assess the relationship between our results and previous single-basin theories, we finally evaluate the sensitivity of the MOC to basin geometry in section 4, before a closing discussion in section 5.

2. Multicolumn model for the MOC

In this section we will briefly review the multicolumn model of JN19 and describe its extension to a multiple basin configuration. The general structure of the model is such that predictive one-dimensional diapycnal advection—diffusion equations for the buoyancy structure in the basins are coupled via diagnostic relationships for the residual overturning streamfunction.

Figure 2 illustrates the model geometry employed in this study as a latitude–depth schematic of the MOC. The schematic is centered on the Southern Ocean, with the Atlantic and Indo-Pacific oceans extending northward to both sides. The model solves for the vertical

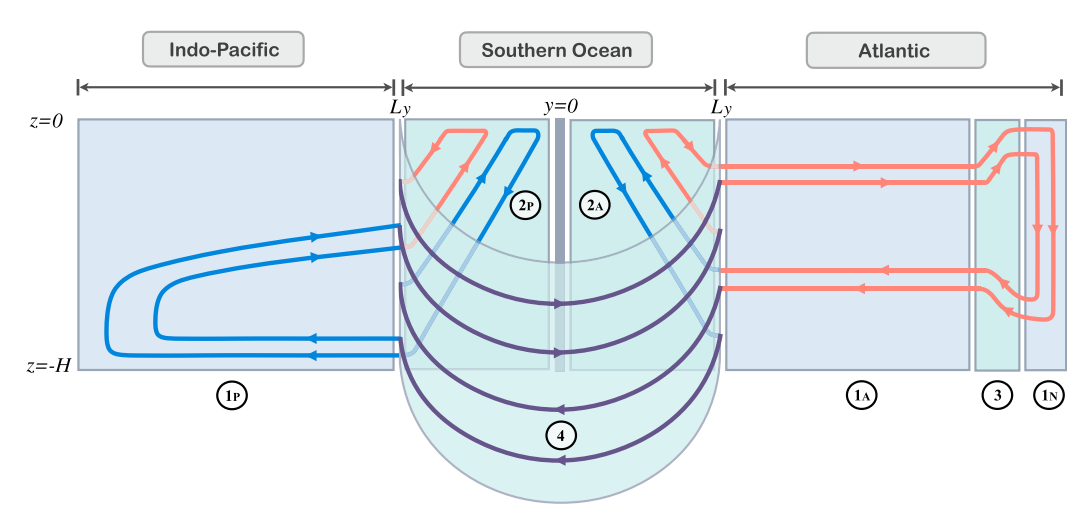


FIG. 2. Schematic of the two-basin column model in a depth-latitude space. The equations solved in the different marked regions are summarized in section 2. The ribbons and associated arrows represent an example circulation.

buoyancy profiles in three different regions: (i) the North Atlantic deep water formation region (labeled 1N), (ii) the Atlantic basin interior (labeled 1A), and (iii) the Indo-Pacific basin interior (labeled 1P). Each of the three vertical buoyancy profiles is represented by a residual-mean advection-diffusion equation described in section 2a. The wind- and eddy-driven meridional overturning streamfunction in each sector of the channel region is computed as described in section 2b (box 2A/2P in Fig. 2, for the Atlantic and Indo-Pacific sectors, respectively), while the overturning streamfunction connecting the Atlantic regions 1N and 1A (box 3 in Fig. 2), as well as the Atlantic and Indo-Pacific basins (box 4 in Fig. 2), are computed using a thermal wind argument described in section 2c.

a. 1D advection-diffusion for the basins

The buoyancy structure in the basins (regions 1A/1N/1P in Fig. 2) evolves according to a residual-mean advection—diffusion equation:

$$\begin{split} \text{Region 1: } & \partial_t b_{(A,N,P)} \approx -w^\dagger_{(A,N,P)} \partial_z b_{(A,N,P)} \\ & + \partial_z \Big(\kappa_{\text{eff}} \partial_z b_{(A,N,P)} \Big) (+\text{conv}). \end{split} \tag{1}$$

Here $w^{\dagger} = w^{\dagger}(b(z))$ is the net residual upwelling across the buoyancy surface b(z), which will be computed from the isopycnal overturning streamfunctions, as discussed in section 3d, and $\kappa_{\rm eff}$ is an effective diapycnal diffusivity profile, which represents the area integrated diffusivity along the isopycnal surface b(z), normalized by the area of the basin (see JN19 for details and derivation). Since the area of isopycnal surfaces is reduced in the bottom boundary layer and vanishes toward the largest density

classes, $\kappa_{\rm eff}$ is tapered to zero over the bottom boundary layer. As discussed in JN19 the vanishing of $\kappa_{\rm eff}$ at the bottom is important to avoid an implied buoyancy flux into the bottom boundary. Outside of the bottom boundary layer, $\kappa_{\rm eff}$ decreases upward, following a hyperbolic tangent profile. Since $\kappa_{\rm eff}$ represents an average diffusivity along isopycnal surfaces, we choose a profile that is slightly smoother than the depth profile that will be applied in the GCM simulation (Fig. 3b).

The last term in Eq. (1) represents a convective adjustment, which is applied for the North Atlantic column (1N in Fig. 2). Convective adjustment is applied as an immediate restoring to a minimum stratification $N_{\min}^2 = 2 \times 10^{-7} \, \mathrm{s}^{-2}$, while keeping the buoyancy at the bottom of the convective depth range fixed at a prescribed value, $b_{N\min}$, which represents the minimum surface buoyancy in the North Atlantic.

b. Circulation in the circumpolar channel

The meridional residual circulation in the Southern Ocean channel (region 2 in Fig. 2) is computed as the sum of the wind- and eddy-driven overturning circulation, following a number of previous studies (Marshall and Radko 2003; Nikurashin and Vallis 2012; Marshall and Zanna 2014). Specifically, we here compute the wind- and eddy-driven contribution to the streamfunction at the southern end of each basin as

Region 2:
$$\Psi_{2(A,P)}(z) = L_{x(A,P)}\left(-\frac{\tau}{\rho_0 f_2} + Ks_{(A,P)}\right),$$
 (2)

where $L_{x(A,P)}$ is the zonal length of the Southern Ocean sector associated with the corresponding basin, and $s_{(A,P)} = \{L_v - y_s(b(z))\}/z$ is the mean isopycnal slope,

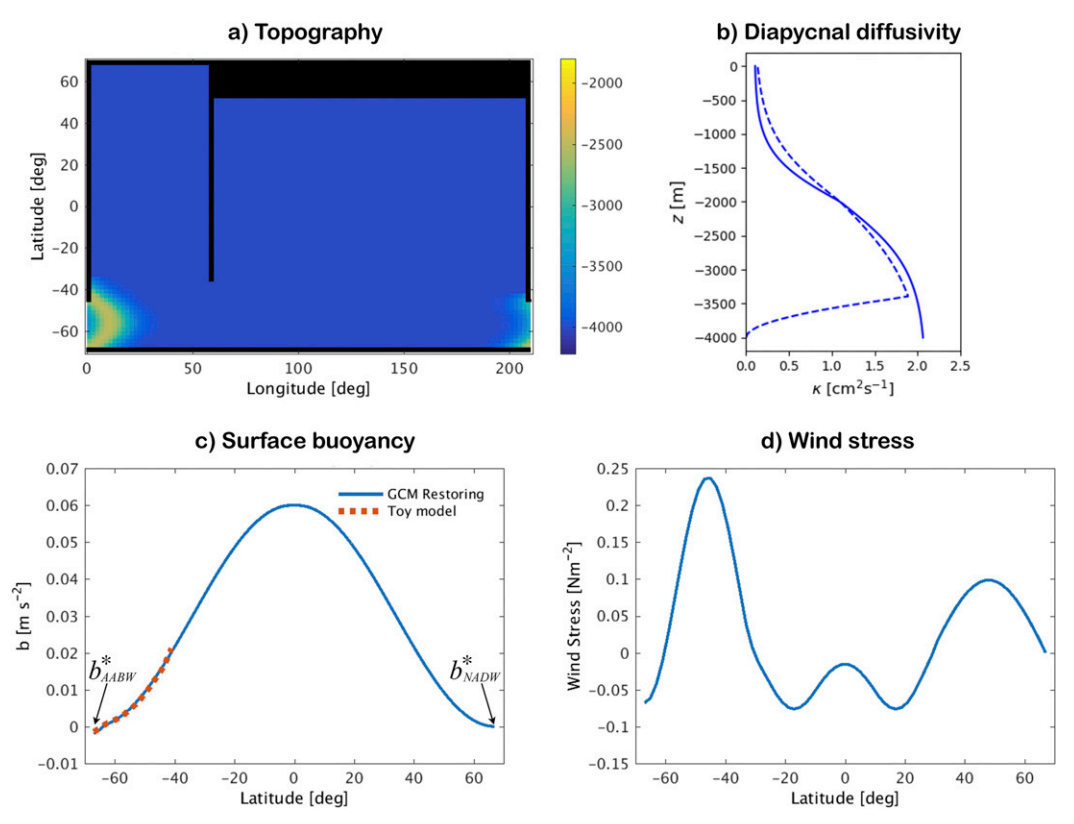


FIG. 3. (a) Geometry used for the GCM simulations; black shaded areas represent landmasses, and color shading indicates seafloor depth. (b) Diapycnal diffusivity profile used for the GCM and toy model. The solid line shows the full diffusivity profile, as used in the GCM, while the dashed line shows the effective diffusivity used in the toy model (see text). (c) Surface buoyancy restoring used in the GCM and toy model and (d) surface zonal wind stress profile used in the GCM.

with $\{L_y - y_s(b(z))\}\$ the meridional distance between the surface outcrop location of the isopycnal b(z) and the northern end of the ACC. We prescribe a zonally symmetric surface buoyancy profile over the Southern Ocean, but allow for the depth of isopycnals to differ between the Atlantic and Indo-Pacific sector, which yields two different isopycnal slopes and correspondingly different overturning streamfunctions in each sector. The term τ is the zonal wind stress, which, for simplicity, is assumed to be constant.

Notice that Eq. (2) provides only the wind- and eddydriven overturning. Since we are treating each sector separately, we generally expect an additional geostrophic transport contribution associated with the zonal pressure contrast across the sector. We will address this contribution separately below.

Rather than considering two separate Southern Ocean sectors, Ferrari et al. (2017) assume a single zonally symmetric Southern Ocean, which connects to the basins via the western boundary of the Atlantic. The assumption that transport into both basins is via the Atlantic western boundary is not well justified in our

simulations (not shown), and an implementation of this approach in our model leads to results that overall match the GCM simulations somewhat less well; although both approaches yield qualitatively similar results.

c. Geostrophic exchange between the columns

Following Nikurashin and Vallis (2012) the overturning circulation in the North Atlantic (region 3 in Fig. 2) is computed using a thermal wind argument:

Region 3:
$$\partial_{zz} \Psi_3^z(z) = -f_3^{-1} [b_A(z) - b_N(z)].$$
 (3)

The same relationship is also applied for the exchange between the Atlantic and Indo-Pacific basin (region 4 in Fig. 2):

Region 4:
$$\partial_{zz} \Psi_4^z(z) = -f_4^{-1} [b_A(z) - b_P(z)].$$
 (4)

Notice that Eq. (4) describes the difference in the baroclinic zonal transport between the Indo-Pacific and Atlantic sectors of the ACC, which in turn is assumed

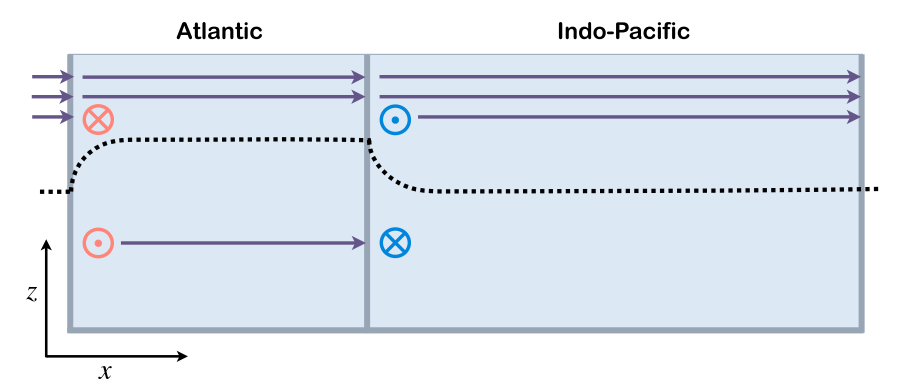


FIG. 4. Sketch indicating the zonal exchange between the two basins through the Southern Ocean channel of the toy model. Deeper isopycnals (indicated by the black dashed line) in the Indo-Pacific vs Atlantic sector imply a stronger baroclinic zonal flow. The mass budget is closed by a baroclinic overturning in and out of the basins along the western boundaries of the continents. Notice that the barotropic (i.e., vertically integrated) zonal flow (which has to be equal in both sectors) has here been chosen arbitrarily for illustration purposes. The model does not predict the barotropic circumpolar flow component, nor do the results for the overturning depend on it.

to be balanced by a meridional geostrophic overturning entering and exiting the two basins along the western boundaries (see sketch in Fig. 4). The thermal wind relationship in Eq. (4) can be viewed as a continuous-coordinate analog to the relationship used for the interbasin exchange in the two-layer model of Ferrari et al. (2017). The boundary conditions for Ψ_3^z and Ψ_4^z are $\Psi_{3/4}^z(z=0) = \Psi_{3/4}^z(z=-H) = 0$, as we assume no net mass transport between the regions.

The residual advection-diffusion equation in (1) requires the isopycnal overturning transport, while Eqs. (3) and (4) provide an estimate of the z-coordinate transport. To compute the isopycnal overturning streamfunctions, Ψ_3^z and Ψ_4^z are mapped into buoyancy space assuming that any transport at depth z occurs at the buoyancy of the respective upstream column:

$$\begin{split} \Psi_{3/4}(b) &= \int_{-H}^{0} \partial_{z} \Psi_{3/4}^{z}(z) \mathcal{H}(b - b_{\rm up}(z)) \, dz \,, \quad \text{where} \\ b_{\rm up}(z) &= \begin{cases} b_{N/P}(z), & \text{if} \quad \partial_{z} \Psi_{3/4}^{z}(z) > 0, \\ b_{A}(z), & \text{if} \quad \partial_{z} \Psi_{3/4}^{z}(z) < 0. \end{cases} \end{split} \tag{5}$$

d. Coupling, boundary conditions, and parameters

The predictive residual advection—diffusion equations for the buoyancy profiles in each region (section 2a), are coupled using the diagnostic relationships for the residual streamfunctions (sections 2b and 2c), which in turn control the advective residual velocities w_A^{\dagger} , w_N^{\dagger} , and w_P^{\dagger} :

$$w_N^{\dagger} = -A_N^{-1} \Psi_3; \quad w_A^{\dagger} = A_A^{-1} (\Psi_3 + \Psi_4 - \Psi_{2A});$$

$$w_P^{\dagger} = A_P^{-1} (-\Psi_4 - \Psi_{2P}), \tag{6}$$

where A_N , A_A , and A_P are the horizontal areas of the respective regions (see Table 1).

Unlike in the setup of JN19, which uses a horizontal advective-diffusive equation for the mixed layer in the Southern Ocean channel, we here simply prescribe the surface buoyancy profile in the Southern Ocean, using a profile that closely matches the GCM simulations (see Fig. 3). In simulations where the AABW density is varied, we adjust the surface buoyancy profile only in the southernmost 5° (555 km), where the profile is linear with a varying slope. The minimum surface buoyancy in the channel region, which we call b_{AABW} , also serves as the bottom boundary condition in the basins. The surface buoyancy in the Atlantic and Indo-Pacific basins is prescribed to match the northern end of the Southern Ocean surface buoyancy profile: $b_{A/P}(z=0) = 0.02 \,\mathrm{m\,s^{-2}}$. The minimum surface buoyancy in the northern deep water formation is set to $b_{N\min} = 3.6 \times 10^{-4} \,\mathrm{m \, s^{-2}}$ (chosen to match the diagnosed minimum northern surface buoyancy in the reference simulation of the GCM).

¹The assumptions for the zonal exchange are also related to those of Thompson et al. (2016), although their model appears to assume that the "baroclinic" flow in each layer, defined as the flow relative to the bottom layer, is proportional to the slope of the interface immediately underlying this layer. This differs somewhat from the thermal wind prediction, according to which the bottom-relative flow would depend on the slopes of all isopycnals between the respective layer and the bottom of the ocean.

TABLE 1. Parameters of the toy model.

$A_A = 7 \times 10^{13} \mathrm{m}^2$	$A_N = 5.5 \times 10^{12} \mathrm{m}^2$	$A_P = 1.7 \times 10^{13} \mathrm{m}^2$
$K = 1800 \mathrm{m}^2\mathrm{s}^{-1}$	$\tau = 0.16 \mathrm{N m^{-2}}$	$\rho_0 = 1030 \mathrm{kg} \mathrm{m}^{-3}$
$L_{xA} = 3714 \mathrm{km}$	$L_{xP} = 9286 \mathrm{km}$	$L_y = 3000 \text{km}$
$f_2 = -1.2 \times 10^{-4} \mathrm{s}^{-1}$	$f_3 = 1.2 \times 10^{-4} \mathrm{s}^{-1}$	$f_4 = 1 \times 10^{-4} \mathrm{s}^{-1}$

Additional model parameters are provided in Table 1 and have been chosen to be consistent with the GCM simulations discussed below. A number of parameters cannot be translated one-to-one due to simplifications in the toy model (e.g., the assumption of a constant wind stress, or the lack of standing meanders, which affect the effective eddy diffusivity). In these cases parameters have been tuned to reproduce the GCM simulation in the reference climate. Specifically, we aimed to roughly match the strength of the overturning and depth of the cell interface at the northern end of the Southern Ocean.

3. Two-basin simulations in GCM and toy model

a. Idealized GCM setup

Results for the column model will be compared to those of a GCM. We will use the MITgcm (Marshall et al. 1997) in various idealized basin configurations. Our reference two-basin geometry is similar to the one used in Nadeau et al. (2019). The domain, shown in Fig. 3a, is a spherical sector, 210° wide in longitude, and extends from 70°S to 70°N in latitude, with a horizontal resolution of $2^{\circ} \times 2^{\circ}$. The domain is 4km deep with 40 vertical layers of varying thickness from 37 m at the surface to 159 m at the bottom. The smaller Atlantic-like basin is 60° wide and extends from 35°S to 70°N, while the larger Indo-Pacific-like basin is 150° wide and extends from 35°S to 54°N. In this reference setup, the areas of the two basins correspond roughly to those of the Atlantic and Indo-Pacific Oceans. Both basins are connected to a Southern Ocean-like region spanning the entire domain south of 35°S. Inside this region, a circumpolar channel opening extends from 70° to 48°S, and is partially blocked by a 2000-m-high Scotia Ridgelike topography, similar to the one used in Ferrari et al. (2017). Other model configurations will be discussed in section 4, where we explore the role of basin geometry. We use a linear equation of state that depends only on temperature, such that buoyancy is given by $b = g\alpha_{\theta}\theta'$, with g the gravitational acceleration, θ' the potential temperature, and $\alpha_{\theta} = 2 \times 10^{-4} \text{ K}^{-1}$ the thermal expansion coefficient. Surface temperature and thus buoyancy at the surface is restored to a zonally symmetric profile with a piston velocity of about 1 m day⁻¹, corresponding to a coupling strength of 50 W m⁻² K⁻¹ (solid blue line in Fig. 3c). For all experiments, the minimum surface restoring buoyancy at the northern end of the Atlantic basin is set to $b_{NADW}^* = 0 \text{ m s}^{-2}$, which thus provides the reference point for our buoyancy variable. The minimum surface restoring buoyancy at the southern end of the domain is $b_{AABW}^* = -0.002 \,\mathrm{m \, s^{-2}}$, in the reference simulation, but will be varied in the sensitivity experiments of section 3d. Notice that the minimum surface restoring buoyancies imposed in the GCM generally do not exactly match the actual diagnosed minimum buoyancies of NADW and AABW, which we denote as b_{NADW} , b_{AABW} and discuss below. The vertical diffusivity profile is horizontally homogeneous and follows a tanh(z) function with inflection point at middepth (solid blue line in Fig. 3b). Values at the surface and the bottom where chosen such that our reference MOC roughly matches that of the ECCO state estimate (Cessi 2019). Momentum input by surface wind stress is represented by the latitudinal profile shown in Fig. 3d. The wind stress over the Southern Ocean is here chosen to be somewhat stronger than in Nadeau et al. (2019) (and also stronger than observed), in order to obtain an upper cell strength and depth in the Southern Ocean that is roughly similar to the results from the ECCO reanalysis (cf. Cessi 2019). The need for an elevated wind stress in the Southern Ocean to obtain a realistic overturning is expected as a result of the shorter ACC (210° as opposed to 360° in the real world), as explained in section 4. Other details about the model configuration can be found in Nadeau et al. (2019).

b. Reference climate results

We first consider results for our reference "present day" model configuration. A comparison of the overturning circulation obtained with the GCM and toy model is shown in Fig. 5 for the depth-averaged MOC and Fig. 6 for the buoyancy-averaged MOC.

The global overturning (right panels) shows the typical overturning structure with two cells stacked on top of each other. In both models the upper cell peaks at around 14 Sv (1 Sv $\equiv 10^6 \,\mathrm{m}^3 \,\mathrm{s}^{-1}$), when averaged in buoyancy coordinates, while the lower cell reaches around 16 Sv in the basin. Significant discrepancies between the GCM and toy model are observed in the latitudes of the circumpolar channel for the depthaveraged MOC (Fig. 5), where a topographically induced standing meander yields closed localized cells in the GCM circulation, but these discrepancies are significantly reduced when the circulation is averaged over isopycnal layers (Fig. 6). Panels on the left show the circulation separated into the Indo-Pacific and Atlantic basins, using a similar layout as Fig. 1, where both basins are plotted as extending outward from the channel. The general structure of the overturning

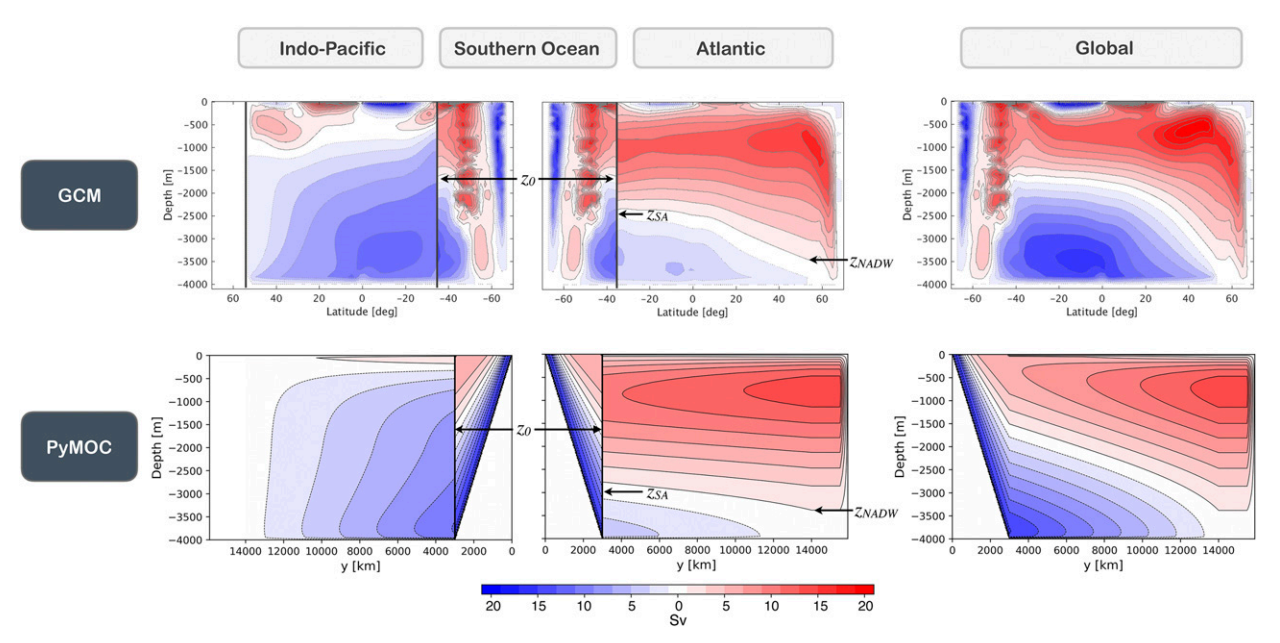


FIG. 5. Meridional overturning circulation (averaged at constant depth) in the (top) GCM and (bottom) toy model. Notice that the Indo-Pacific is mirrored, with north on the left. In the latitude range of the Southern Ocean all panels show the global overturning. The contour interval is $2 \, \text{Sv}$, with white shading for $-1 \, \text{Sv} < \Psi < 1 \, \text{Sv}$.

resembles the observations (Lumpkin and Speer 2007), although the depth-averaged circulation in Fig. 5 shows two shallow clockwise overturning cells (absent from observations) in the north and south of the Pacific basin. These result from a smaller-than-observed northern surface buoyancy and a stronger-than-observed channel

wind stress, respectively. The shallow cells do not appear in the buoyancy-averaged overturning (Fig. 6) and are therefore not expected to affect our main results.

In both models, an overlap between the Atlantic upper cell and Indo-Pacific lower cell is visible over a wide range of depths and buoyancies. To characterize

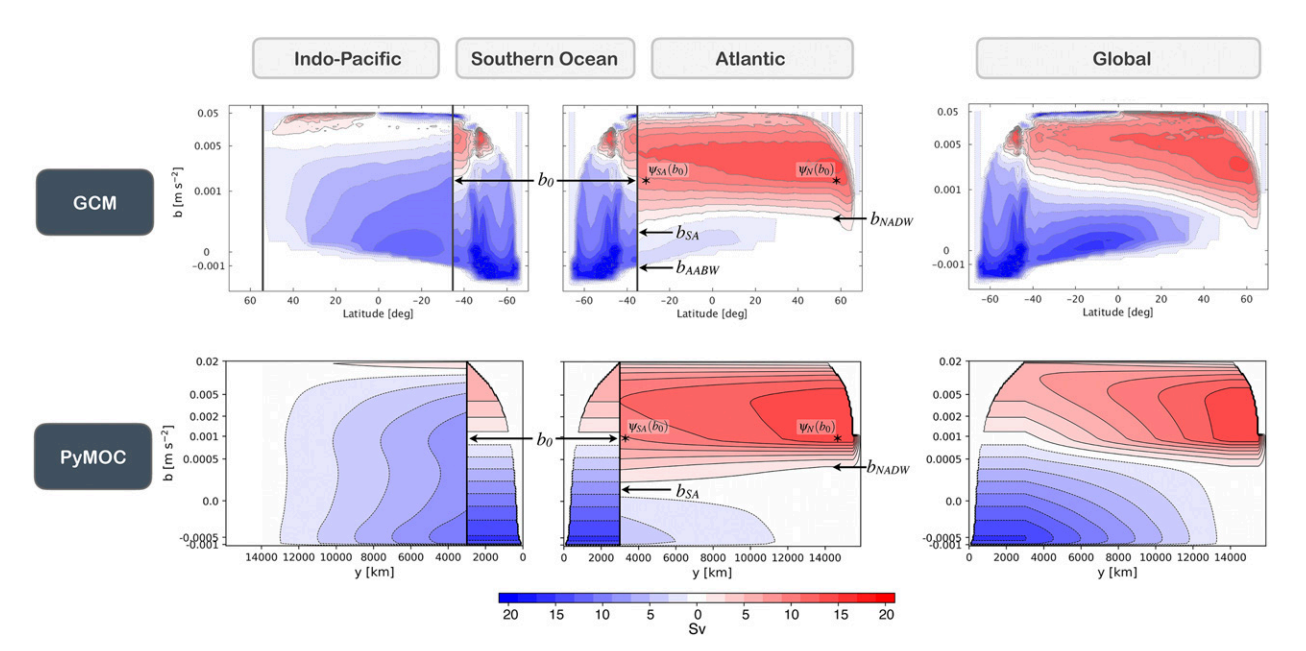


FIG. 6. As in Fig. 5, but for the isopycnal overturning circulation. The vertical axis is scaled according to the globally averaged isopycnal depth. The asterisks denote the locations where $\Psi_{SA}(b_0)$ (the isopycnal overturning at b_0 in the South Atlantic) and $\Psi_N(b_0)$ (the isopycnal overturning at b_0 in the North Atlantic) are defined, where b_0 is the isopycnal that separates the upper and lower global overturning cell at the northern end of the Southern Ocean (see text).

the exchange of properties between the two cells, we interpret our results in terms of the pathways discussed in Fig. 1, which highlight the importance of the isopycnals b_0 and b_{NADW} . In contrast to the schematics of Fig. 1, however, our results also include diapycnal effects in the Atlantic interior. As a result, we will focus our analysis on three isopycnal surfaces (Fig. 6): (i) b_{NADW} is the minimum buoyancy corresponding to the upper cell in the north of the Atlantic basin, 2 (ii) b_{SA} is the minimum buoyancy of the upper cell in the south of the Atlantic basin, and (iii) b_0 marks the buoyancy where the global-integrated streamfunction changes sign at the northern end of the Southern Ocean region. For the depth averaged circulation (Fig. 5), we similarly define z_{NADW} , z_{SA} , and z_0 . Notice that although the base of the AMOC shoals southward in depth space ($z_{SA} > z_{NADW}$), the minimum buoyancy of southward flowing NADW actually decreases toward the channel ($b_{SA} < b_{NADW}$), that is we find diabatic "downwelling" in the Atlantic near the bottom of the AMOC cell. At shallower depth, we instead see diabatic upwelling. The diabatic component in the Atlantic therefore tends to spread NADW, which initially occupies a relatively tight range of buoyancies, as it moves southward in the Atlantic basin.³

The cell "overlap" is here defined as the transport out of the Atlantic in the range of overlapping buoyancies $b_0 < b < b_{SA}$, which is measured by $\psi_{SA}(b_0)$ (cf. Nadeau et al. 2019; Baker et al. 2020). This transport, which in the reference simulation amounts to $\psi_{SA}(b_0) \approx 9 \,\text{Sv}$, is associated with the conveyor mode of the AMOC, and is critical for pathways 4 and 5 in Fig. 1. Notice that $\psi_{SA}(b_0)$ must be balanced by a similar diabatic upwelling across b_0 in the Indo-Pacific in order to close the mass budget, and hence could similarly be diagnosed in terms of the overturning streamfunction at b_0 at the southern end of the Indo-Pacific. The overlap is closely related to the full diabatic extension of the AMOC, which we here define as the net overturning transport in the North Atlantic that extends past the minimum buoyancy of adiabatic upwelling in the SO, i.e., $\psi_N(b_0)$.

To further illuminate the role of the adiabatic versus diabatic pathways, it is useful to isolate those components explicitly. In the toy model, such a decomposition is relatively straightforward, as water mass transformations are limited to four distinct regions: the northern deep water formation region, the Southern Ocean, and the interiors of each basin. The adiabatic component, by definition, is not associated with any interior transformations, and can thus be identified as the part of the northern sinking (across any given buoyancy surface *b*) that is balanced by an opposite transformation (across the same density surface) in the SO:

$$\Psi_3^{\text{adia}}(b) = \Psi_2^{\text{adia}}(b) = \min(\Psi_3^+(b), \Psi_2^+(b)),$$
 (7)

where $\Psi^+=\max(\Psi,0)$ is the positive (clockwise) part of the overturning (there is no adiabatic contribution to the counterclockwise circulation, as all sinking in the SO is balanced by diffusive upwelling), and $\Psi_2=\Psi_{2A}+\Psi_{2P}$ is the total overturning in the adiabatic Southern Ocean. Hence, $\Psi_2^+(b)$ is the total adiabatic upwelling (as a function of b) in the Southern Ocean, and in practice $\Psi_{2/3}^{\rm adia}(b)=\Psi_2^+(b)$ on most buoyancy surfaces. However, on some buoyancy levels in the upper ocean $\Psi_2^+(b)>\Psi_3^+(b)$, that is Southern Ocean upwelling is partially balanced by diabatic downwelling in the basins (as opposed to surface transformation in the North Atlantic). This component is hence removed in our definition of the adiabatic overturning.

The overturning circulation that remains after subtracting the adiabatic component is purely diabatic in the sense that at least one of the transformations (from dense to light or from light to dense) occurs diffusively in the interior:

$$\Psi_{2/3}^{\text{dia}}(b) = \Psi_{2/3}(b) - \Psi_{2/3}^{\text{adia}}(b). \tag{8}$$

As illustrated in Fig. 7, the adiabatic circulation consists of an interhemispheric clockwise cell, confined to the Atlantic basin. This circulation resembles the adiabatic upper cell mode sketched in the first row of Fig. 1.

The remaining diabatic circulation resembles to a large part the full diabatic pathway sketched in the

 $^{^2}$ Notice that, in practice, we here define $b_{\rm NADW}$ as the depth where Ψ first drops below 1 Sv at 56°N. Since there is no abyssal cell in the North Atlantic, the actual zero-crossing of the streamfunction (used for the definition of b_0 and $b_{\rm SA}$) is poorly defined.

³ As discussed by Wolfe and Cessi (2011) for the adiabatic limit, injection of NADW in the north forms a "thermostat" of weakly stratified water. Diffusive mixing weakens this thermostat while driving up- and downwelling out of the weakly stratified depth range.

⁴The cell overlap, $\psi_{\rm SA}(b_0)$, is similar to the "lower branch" of the NADW flowing below $\sigma_{\rm ice}$ as defined in Nadeau et al. (2019) and similar to the quantity "NADW_pac_lower" defined in Baker et al. (2020).

⁵Notice that, even in the toy model, the definition of the adiabatic contribution is not generally strictly unambiguous, as any diabatic circulation component with surface transformation in one hemisphere could be formulated as the sum of an interhemispheric adiabatic circulation plus a diabatic component with surface transformation in the opposite hemisphere. However, only the definition in (7) guarantees no cancelling diabatic and adiabatic contributions at any given buoyancy and region.

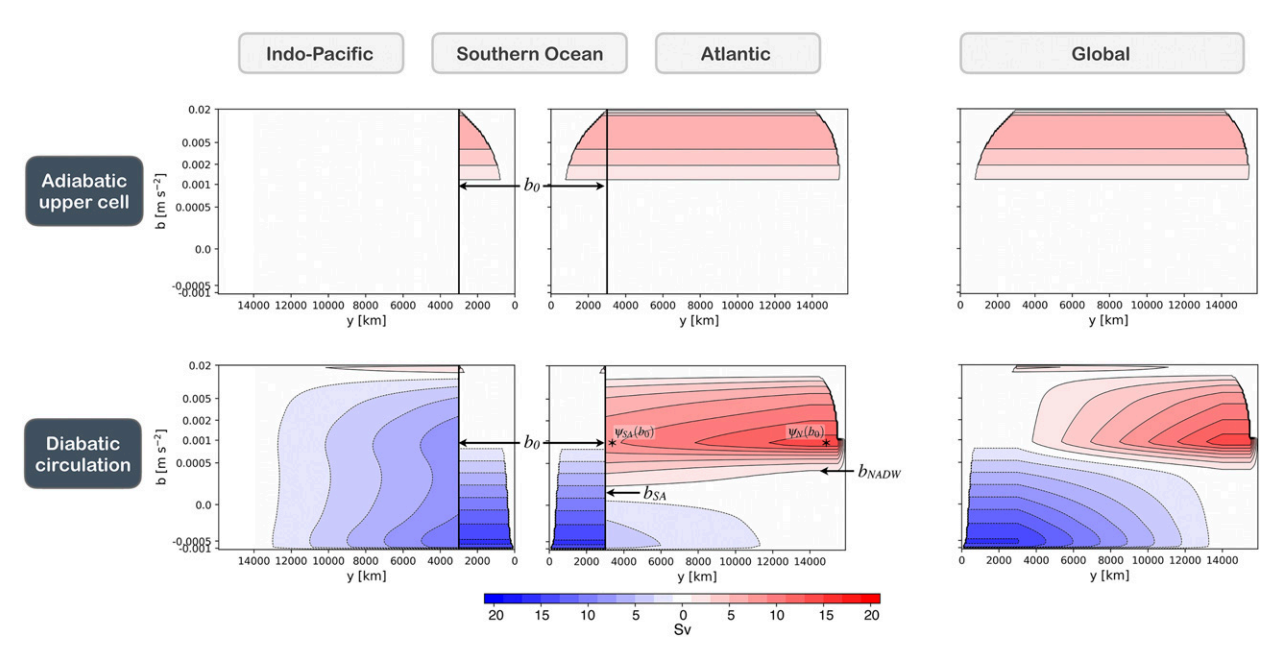


FIG. 7. (top) Adiabatic component of the isopycnal overturning in the toy model (cf. Fig. 1, row 1). (bottom) Diabatic component of the overturning (cf. Fig. 1, row 4).

fourth row of Fig. 1 and includes the lower cell, associated with the recirculation of AABW (cf. row 2 in Fig. 1), as well as the diabatic component of the upper cell, associated with the diabatic recirculation of NADW (cf. row 3 in Fig. 1). Notice that the diabatic contribution to the upper cell, throughout the meridional length of the Atlantic, has its maximum value near b_0 (bottom row in Fig. 7). The diabatic component of the upper cell is hence extending the upper cell below the depth of the adiabatic contribution, which by definition goes to zero at b_0 . This diabatic extension of the upper cell is critical for the existence of a cell overlap.

c. Role of diapycnal diffusivity and surface buoyancy boundary conditions

Our reference experiment is meant to represent the present-day MOC, which shows a wide range of overlapping buoyancies (e.g., Lumpkin and Speer 2007; Talley 2013; Cessi 2019). However, proxy data of the LGM suggest that this overlap was much smaller than it is today, as a result of stratification and circulation changes. An emerging consensus on the mechanisms responsible for these changes points to the role of Antarctic sea ice in controlling the depth of the AMOC, by modulating surface buoyancy loss around Antarctica (e.g., Shin et al. 2003; Ferrari et al. 2014; Jansen and Nadeau 2016; Marzocchi and Jansen 2017). Nadeau et al. (2019) and Baker et al. (2020) recently showed that an increased latitudinal sea ice extent and increased rate of Antarctic sea ice formation can result in a shoaling of the AMOC

and a significant reduction of the overlap between the two cells of the MOC. Moreover, we argue above that the cell overlap critically depends on the diabatic extension of the upper cell, which suggests that diapycnal diffusivity is likely to play a key role in controlling the depth of the AMOC and the exchange between the two cells.

Here, we will systematically explore the sensitivity of the circulation, and in particular the cell overlap, on both the buoyancy of AABW and the diapycnal diffusivity. Changes in the buoyancy of AABW can be thought of as representing changes in brine rejection from sea ice formation and export around Antarctica. This process has likely differed substantially during the LGM, and is also likely to be poorly represented in GCM simulations of the present-day overturning. Similarly, diapycnal mixing rates remain very poorly constrained and may have differed substantially in the LGM (e.g., Schmittner et al. 2015). Diapycnal mixing rates are here modified by simply multiplying the diffusivity profile of the reference simulation by varying factors. The density of AABW is varied by modifying the surface density in a small strip around Antarctica while keeping it fixed elsewhere (cf. section 3a). Importantly, this implies that we are directly varying the buoyancy contrast between NADW and AABW, thus affecting the abyssal stratification, which has previously been argued to play a key role in controlling the depth of the AMOC (Jansen and Nadeau 2016).

We first illustrate the effect of increased diapycnal diffusivity and reduced AABW buoyancy by doubling

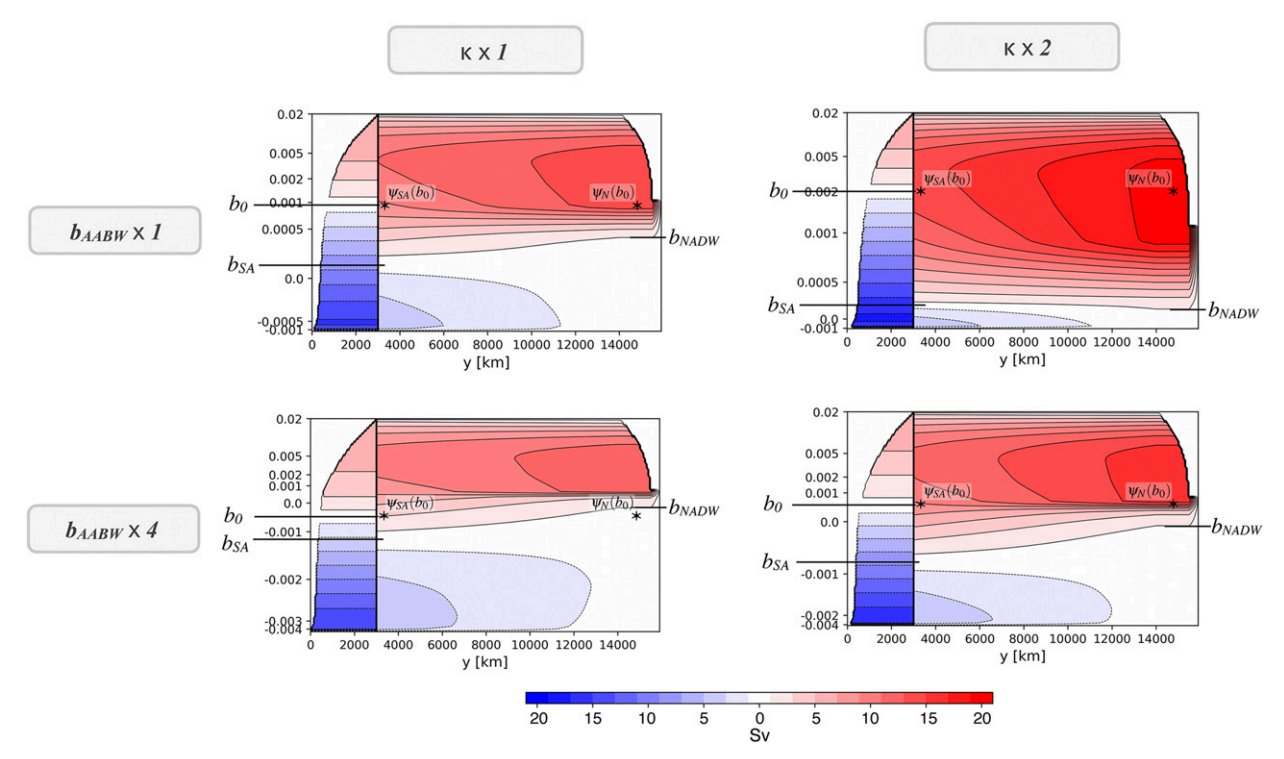


FIG. 8. Isopycnal overturning in the Atlantic and Southern Ocean in the toy model for the (top left) reference case, (right) doubled diapycnal diffusivity, and (bottom) quadrupled minimum (negative) AABW buoyancy (which approximately amounts to a quadrupling of the buoyancy contrast between AABW and NADW). Increased diapycnal diffusivity leads to a deepening of the AMOC and an increased cell overlap, while greater AABW density leads to a shoaling of the AMOC and reduction in the overlap. The two effects largely compensate in the bottom-right panel, leading to a similar overlap as in the control case.

the diapycnal diffusivity and quadrupling b_{AABW} in the toy model. (Notice that b_{AABW} is negative and all buoyancies are relative to $b_{\rm NADW}^* \equiv 0$). The results are summarized in Fig. 8, where the upper-left panel reproduces the circulation obtained for the reference present-daylike experiment (same as in Fig. 6), while the lower-left panel shows the effect of a fourfold increase in the magnitude of b_{AABW} . Similarly to the results of Nadeau et al. (2019), the upper cell in the Atlantic shoals substantially if the buoyancy of AABW is reduced, while the global average circulation in the SO changes much less. (Notice that the vertical axis in the figure is scaled by the mean depth of the respective isopycnal, and thus contains depth information.) In other words, both b_{NADW} and b_{SA} are shifted upward while the average depth of b_0 remains relatively unchanged. The range of shared buoyancies, $b_0 < b < b_{\text{SA}}$, and the overlap, $\psi_{\text{SA}}(b_0)$, are thus both reduced. The opposite response is observed for a twofold increase in vertical diffusivity (right panel of Fig. 8), where the diabatic transport increases roughly by a factor of 2. The combined effect of reduced b_{AABW} and increased κ yields a circulation similar to the reference experiment, albeit with a stronger abyssal stratification (lower-right panel).

We now explore the sensitivity of the circulation to diffusivity and AABW buoyancy over a wide parameter range. We use the toy model to explore the full two-dimensional κ - $b_{\rm AABW}$ parameter space using 13 increments of κ/κ_0 from 0.1 to 3.0 and 13 increments of $b_{\rm AABW}$ from -0.0084 to $-0.00036\,\mathrm{m\,s^{-2}}$, for a total of $13\times13=169$ solutions. The main results are confirmed using two series of GCM simulations. One set where the minimum surface restoring buoyancy around Antarctica is varied using $b_{\rm AABW}^*=0$, (-0.002), -0.004, -0.006, -0.008, and $-0.01\,\mathrm{m\,s^{-2}}$ (where the value in parenthesis refers to the reference simulation), while κ is held fixed at its reference profile, and one set of simulations with varying $\kappa/\kappa_0=0.25$, 0.5, (1), and (2), where $b_{\rm AABW}^*$ is held fixed at the reference value.

As previously indicated by the illustrative cases in Fig. 8, we find that the depth of NADW in the Atlantic (as measured by both $z_{\rm NADW}$ and $z_{\rm SA}$) increases systematically with increasing κ or increasing $b_{\rm AABW}$ (Figs. 9a,b). The depth of zero global overturning in the Southern Ocean channel, z_0 , instead is relatively weakly sensitive (Fig. 9c), which leads to a systematic increase of the shared depth range. The deepening of NADW (relative to z_0) with increasing diapycnal diffusivity is consistent

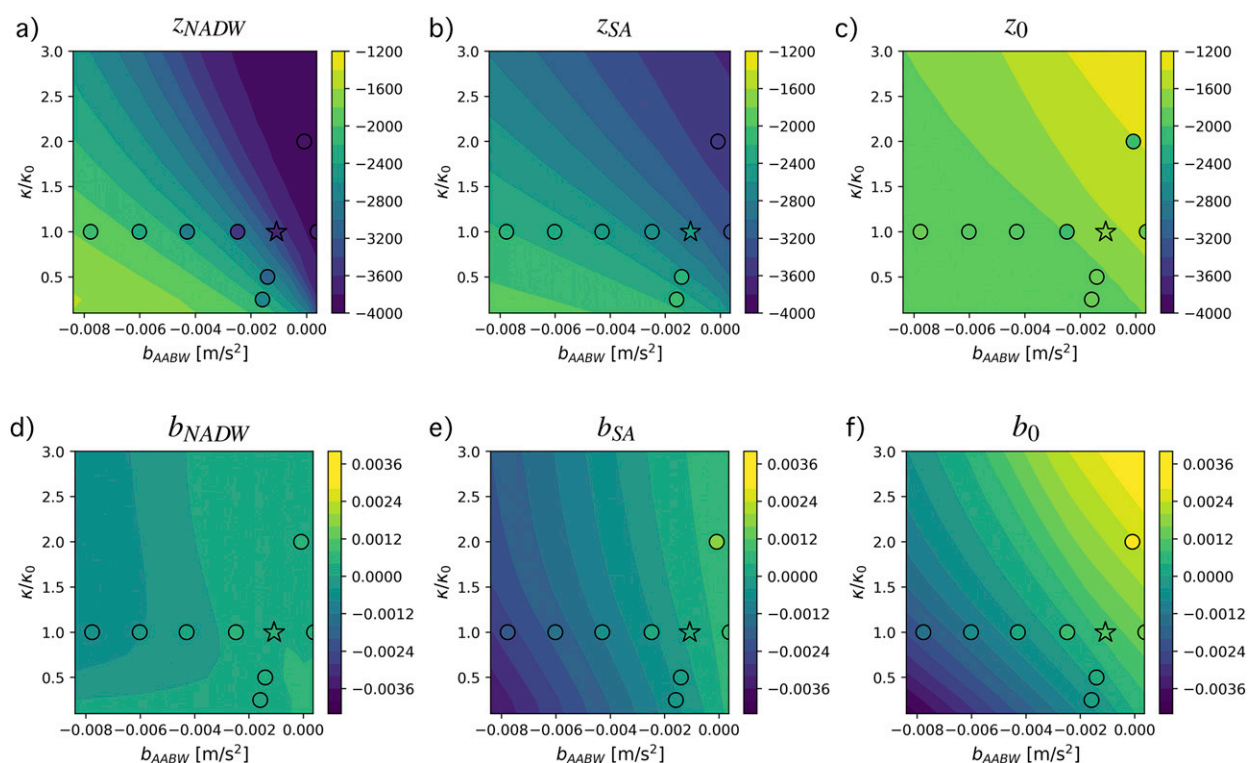


FIG. 9. (a)—(c) Depth of the upper cell in the North Atlantic, $z_{\rm NADW}$, at the southern end of the Atlantic basin, $z_{\rm SA}$, and in the Southern Ocean, $z_{\rm 0}$, as a function of the AABW buoyancy $b_{\rm AABW}$ and the magnitude of the diapycnal diffusivity (normalized by the diffusivity in the reference simulation). (d)—(f) Corresponding buoyancies denoting the bottom of the upper cell in isopycnal coordinates (cf. Figs. 5 and 6). Shading shows the toy model results and filled markers indicate results from the GCM simulations, with the stars marking the present-day-like reference case for which $b_{\rm AABW} = -0.0011$ m s $^{-2}$ and $\kappa/\kappa_0 = 1$. In the GCM, $b_{\rm AABW}$ is diagnosed as the bottom buoyancy at the northern end of the Southern Ocean, which is generally larger than the prescribed minimum restoring buoyancy $b_{\rm AABW}^*$ due to surface disequilibrium and interior diabatic transformations within the Southern Ocean, neither of which are included in the toy model.

with the fact that this lower part of the upper cell is inherently controlled by diabatic processes (cf. section 3b). The deepening of NADW with increasing AABW buoyancy is consistent with the results of Jansen and Nadeau (2016), as an increase in $b_{\rm AABW}$ leads to a reduction of the abyssal buoyancy contrast ($b_{\rm NADW}-b_{\rm AABW}$), and thus a reduction of the abyssal stratification, which was shown to lead to an expansion of the AMOC.

The deepening of NADW but comparatively weak sensitivity of z_0 to increasing κ or increasing b_{AABW} is robust across the GCM and toy model, although a couple of notable differences exist (see also Fig. S1 in the online supplemental material). First, z_{NADW} is generally deeper in the GCM compared to the toy model, except in the limit of very buoyant AABW where z_{NADW} extends essentially to the bottom of the ocean. The too-shallow NADW in the toy model likely results from the model's inability to represent the meridional bottom buoyancy gradient in the Atlantic basin, which leads to higher abyssal North Atlantic buoyancies in the GCM, allowing for a deeper penetration of NADW. Second,

the response of z_0 to changes in κ , although weak in both models, is of opposite sign. While z_0 slightly deepens in response to increased κ in the GCM, it actually shoals in the toy model. The slight shoaling of z_0 in the toy model can be understood by noting that increased κ leads to a deepening of isopycnals in the basin, and hence a steepening of isopycnal slopes in the channel (as the surface buoyancy distribution in the Southern Ocean is fixed). The steepening of isopycnals leads to a strengthening of the eddy-driven, counterclockwise, circulation, which then leads to an expansion of the lower (counterclockwise) and contraction of the upper (clockwise) cell. While it is not entirely clear why this response is not observed in the GCM, matters are clearly complicated due to the fact that the surface buoyancy in the Southern Ocean is not fixed, but constraint less strongly by the surface restoring boundary condition, and the residual circulation is strongly affected by standing meanders whose response to changes in the mean state is more complex.

As we are ultimately most interested in the isopycnal overturning, it is also instructive to consider changes in

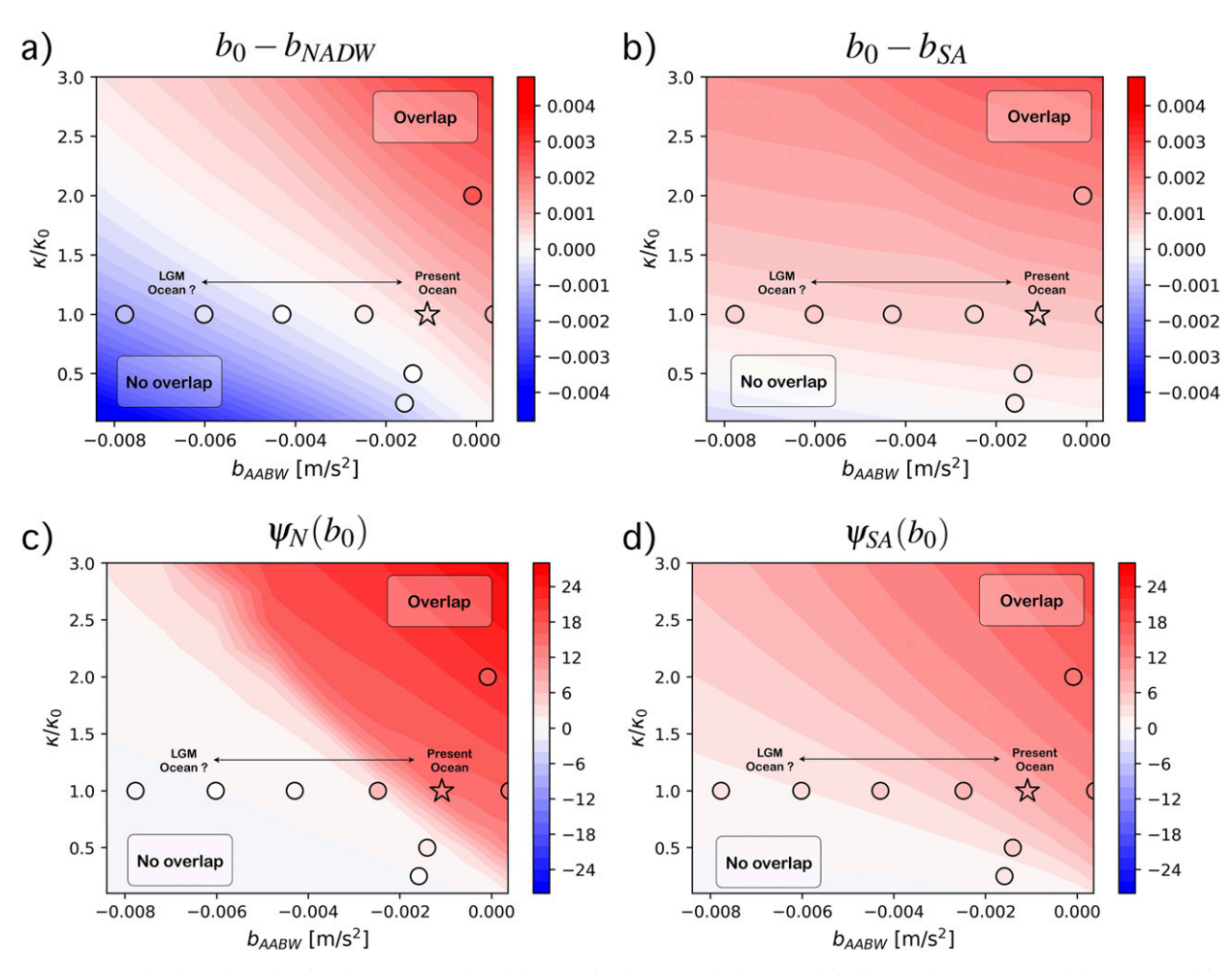


FIG. 10. As in Fig. 9, but showing the range of shared buoyancies between the lower cell in the Southern Ocean and the upper cell in (a) the North Atlantic and (b) the South Atlantic, as well as (c) the diabatic extension of the AMOC in the North Atlantic and (d) the cell overlap in the South Atlantic. (cf. Fig. 6). The arrows qualitatively indicate the potential shift in parameter space between the present and LGM, where enhanced Antarctic buoyancy loss likely led to an increased buoyancy contrast between AABW and NADW.

the actual buoyancies of the isopycnals b_{NADW} , b_{SA} , b_0 . From this perspective, we find that it is instead b_0 that is most sensitive and increases in response to increased diffusivity or b_{AABW} (Figs. 9d-f). The sensitivity of b_0 can be understood by noting that (for a fixed wind stress and eddy diffusivity) the wind- and eddy-driven streamfunction goes through zero at an approximately fixed depth, associated with a certain critical isopycnal slope. The buoyancy at this depth, however, increases with increased diffusivity or increased b_{AABW} . The minimum buoyancy of NADW, b_{NADW} , instead changes relatively little, as it is tightly constraint by the minimum surface buoyancy in the North Atlantic. As a result, we find a systematic increase in the range of overlapping buoyancies $(b_0 - b_{NADW})$ with increasing diffusivity or b_{AABW} (Fig. 10a). The diabatic extension of the AMOC in the north of the Atlantic, $\psi_{\rm N}(b_0)$, then increases sharply as $(b_0 - b_{NADW})$ becomes positive, such that NADW is injected at densities that are no longer part of the upper cell in the southern channel (Fig. 10c). The diabatic spreading of NADW in the Atlantic effectively smooths this sharp transition, but the same qualitative response applies to the range of overlapping buoyancies at the southern end of the basin. That is, $b_{\rm SA}$ responds much less strongly than b_0 to an increase in κ or $b_{\rm AABW}$, leading to an increase in the range of shared buoyancies ($b_{\rm SA}-b_0$) and a resulting increase in the overlap $\Psi_{\rm SA}(b_0)$.

The sensitivity of $b_{\rm NADW}$, $b_{\rm SA}$, and b_0 , as well as the resulting AMOC extension $\Psi_N(b_0)$ and overlap $\Psi_{\rm SA}(b_0)$, are generally consistent between the toy model and GCM simulations (see also Figs. S2 and S3 for a direct comparison of GCM versus toy model results). Naturally, the GCM simulations, however, do not cover the entire parameter regime explored with the toy model such that some caution is required when interpreting the toy model

results outside the parameter range considered in the GCM simulations.

For values of diffusivity in the vicinity of the reference case, reducing b_{AABW} allows for a transition from a present-day-like circulation, characterized by a strong overlap, to an LGM-like circulation, characterized by a weak overlap, as previously discussed by Nadeau et al. (2019)⁶ and Baker et al. (2020). The model, however, also highlights the potentially important role of changes in the diapycnal diffusivity. Significant changes in the diffusivity between the present-day and LGM are possible, although the magnitude and even direction of change remains uncertain. The reduced area of shelf seas likely led to higher tidal energy dissipation in the deep ocean, which provides a key energy source for diapycnal mixing (e.g., Schmittner et al. 2015). Enhanced abyssal stratification associated with reduced AABW buoyancy, however, also implies that more energy is needed to generate diapycnal mixing (e.g., Wunsch and Ferrari 2004), which leaves the net change in the diapycnal diffusivity highly uncertain. Our results show that strongly increased diapycnal mixing could counteract the effect of reduced AABW buoyancy, perhaps causing relatively little change in the cell overlap between the present-day and LGM circulation. Reduced diapycnal mixing instead could further enhance the circulation changes caused by reduced AABW buoyancy, potentially leading to a complete elimination of any cell overlap.

4. The role of basin geometry

Much progress has been made toward a theoretical understanding of the deep ocean overturning circulation using single-basin models (Gnanadesikan 1999; Wolfe and Cessi 2009; Nikurashin and Vallis 2011, 2012; Wolfe and Cessi 2011; Jansen and Nadeau 2016; JN19). The results above, however, highlight the role of interbasin exchange, including the importance of diapycnal upwelling in the Indo-Pacific to balance sinking in the North Atlantic. This raises the question of what, if anything, we can still learn from single-basin theories. In the following, we will illustrate that single-basin models and theories remain powerful tools to understand the global overturning circulation even in multibasin configurations, if we adequately account for the global ocean area and length of the circumpolar channel.

We first compare the difference in the deep ocean overturning circulation between our two-basin model and a single-basin configuration, by simply removing the continental strip that separates our two basins, which leads to a single-basin geometry with similar global ocean area and circumpolar channel length. As shown in Fig. 11 (first and second row), the global MOC is very similar with and without a separation between the two basins, which suggests that the global overturning is to zeroth-order independent of how the area is distributed over basins.

The similarity of the global MOC between simulations with and without a continent separating the ocean into two basins can be understood with the help of the toy model by considering the limit case of efficient basin exchange, which can formally be achieved by taking the limit $f_4 \rightarrow 0$. In this limit, Eq. (4) requires that $b_P = b_A \equiv$ $b_{\rm basin}$ for any finite Ψ_4 (whose magnitude is limited by the capacity for diabatic upwelling in the Indo-Pacific and sinking in the channel and North Atlantic). The evolution equation for the basin buoyancy b_{basin} can then be obtained by adding the advection-diffusion equations for each basin, which yields an equation identical to (1) but with $b_{(A,N,P)} \rightarrow b_{\text{basin}}$ and $w_{(A,N,P)}^{\dagger} \rightarrow w_{\text{basin}}^{\dagger} =$ $(A_P + A_A)^{-1}(\Psi_3 - \Psi_2)$. The overturning circulation Ψ_3 follows as before from Eq. (3) with $b_A \rightarrow b_{\text{basin}}$ and the total meridional overturning in the channel, $\Psi_2 = \Psi_{2A} + \Psi_{2P}$, is given by an equation identical to (2) with $s_{A,P} \rightarrow s_{\text{basin}}$ (identical in both sectors) and $L_{x(A,P)} \to L_{xA} + L_{xP}$. The equations for the global overturning circulation thus become identical to those of a single-basin model with a basin area $A = A_P + A_A$ and channel length $L_x = L_{xA} +$ L_{xP} (cf. JN19). Indeed, we could also deduce the overturning through the two basins from the single-basin solution, by noting that, in the limit where $b_A \approx b_P$, both the overturning in the channel and the diapycnal upwelling in the basins are simply distributed across the two sectors/basins in proportion to their respective length/area. In reality, the exchange between the two basins of course is not infinitely efficient, and as a result the buoyancy profiles in the two basins are not identical (cf. Thompson et al. 2016; Ferrari et al. 2017). Nevertheless, this limited case provides a useful framework for a zeroth-order understanding of the global overturning in a multibasin model, as illustrated by the results in Fig. 11.

Importantly, the results above do not suggest that the Atlantic MOC (or the upper cell) is to zeroth-order unaffected by the Indo-Pacific, as becomes clear if the Indo-Pacific basin is replaced with land (third row of Fig. 11). In the absence of diapycnal upwelling of former NADW in the Indo-Pacific, the diabatic portion of the AMOC vanishes almost completely. The large reduction

 $^{^6}$ Notice that in addition to increased sea ice formation and export, which leads to a reduction in $b_{\rm AABW}$, Nadeau et al. (2019) also identified sea ice extent as a parameter that can control the overlap. For simplicity, this parameter was fixed here and further work is needed to evaluate its influence on the parameter space presented in Figs. 9 and 10.

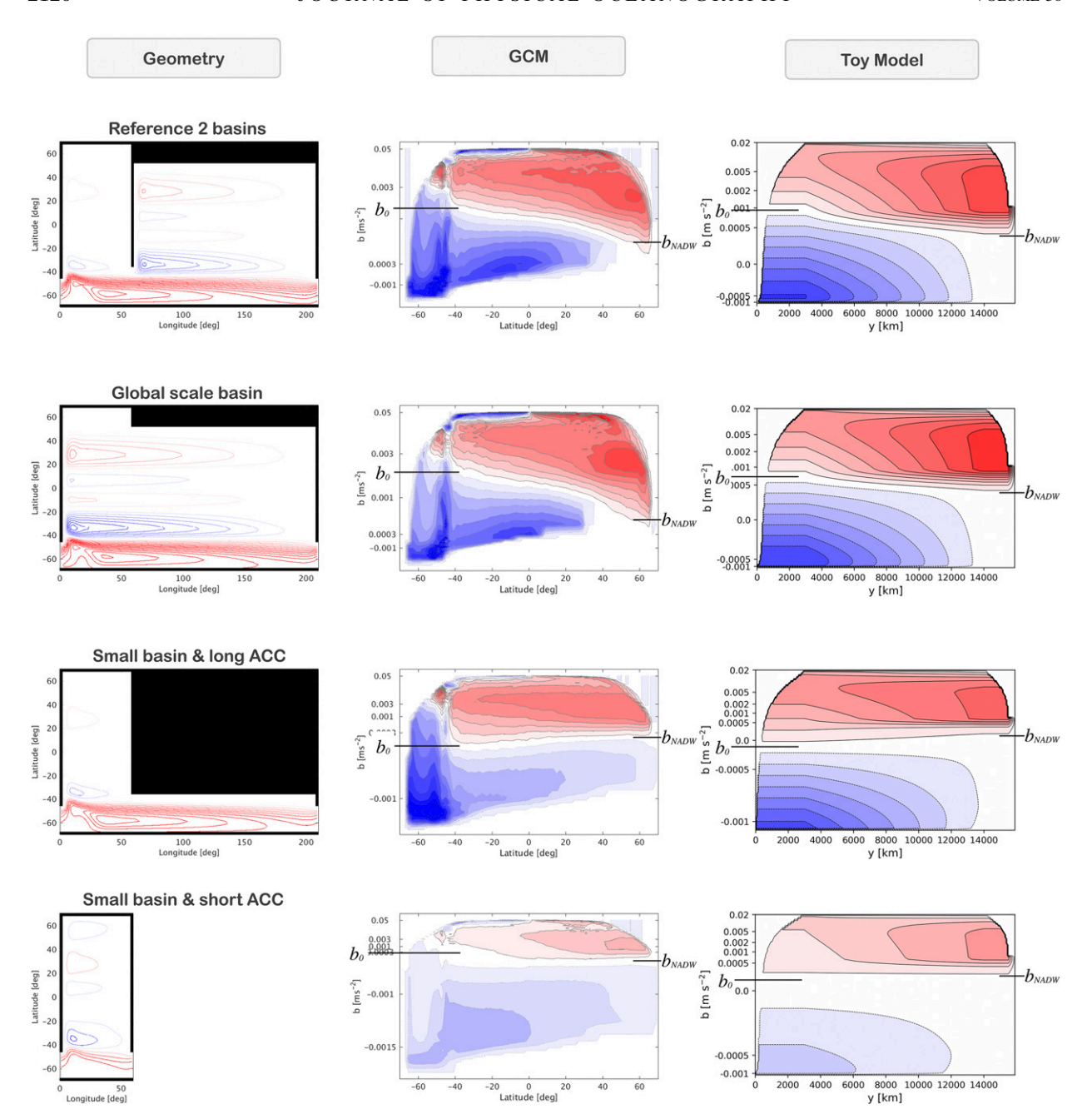


FIG. 11. Global overturning in (center) the GCM and (right) the toy model for (left) various geometries: (first row) reference experiment; (second row) as in the reference experiment, but without a separation between the two basins; (third row) as in the reference experiment, but with the Indo-Pacific filled with land; and (fourth row) as in the third row, but with reduced channel length. Contours in the left panels show the barotropic streamfunction in the GCM (one streamline corresponds to 15 Sv).

of the basin area over which diffusive upwelling occurs is similar to the response to a decrease in diapycnal diffusivity, as can readily be seen from the toy model, where the basin area effectively appears only in product with the diapycnal diffusivity, in the steady state solution. [This can be seen by inserting the relationships in Eq. (6) into Eq. (1).] The reduced area of diffusive

upwelling hence leads to an elimination of the diabatic extension of the AMOC and hence a shoaling of North Atlantic Deep Water, $z_{\rm NADW}$. This shoaling of NADW occurs without a significant change in the depth of the isopycnal associated with the zero streamfunction in the channel (z_0), thus eliminating the shared depth and buoyancy range between the upper and lower cell. The smaller

area-integrated diapycnal diffusivity further yields a somewhat weaker abyssal stratification and circulation.

Last but not least, the global MOC is controlled by the total length of the channel (last row of Fig. 11). If the channel length is reduced to the width of the Atlantic basin, the Southern Ocean overturning is significantly weaker [recall that $\Psi_2 \propto L_x$ in Eq. (2)]. This results in a reduction of the adiabatic portion of the AMOC (cf. the third and fourth rows of Fig. 11). The channel's length also impacts the eddy-driven circulation in the abyssal cell, as well as the area integrated negative buoyancy flux at the surface of the channel, affecting the strength and stratification of the abyssal cell (cf. Jansen and Nadeau 2016).

These results highlight that common biases in idealized single basin simulations, including a relatively weak and shallow AMOC, can be understood directly as a result of the reduced domain size, which leads to reduced diabatic and adiabatic upwelling. When the real ocean area and length of the Southern Ocean are accounted for, single-basin theories, however, remain useful to provide a zeroth-order understanding of the global ocean overturning. Notice also, that although the two overturning cells by definition have to close on each other in a single-basin model, the two cells can still have a shared density range (i.e., $b_{NADW} > b_0$)—as illustrated by the "global scale basin" case in Fig. 11. This shared buoyancy range is likely to be critical to the intercell exchange of tracers, even in a single basin model, as it allows for along-isopycnal mixing between the two cells by eddies and gyres (e.g., Burke et al. 2015; Jones and Abernathey 2019; Nadeau et al. 2019), while any intercell mixing is limited to diapycnal processes when the shared buoyancy range is eliminated.

5. Summary and conclusions

We have extended the toy model for the meridional overturning circulation of JN19 to include an interbasin exchange between two basins connected via a Southern Ocean channel. The model was used to explore and understand the sensitivity of the overturning circulation to external parameters, specifically the diapycnal diffusivity and the interhemispheric contrast in minimum surface buoyancy. A particular focus of our study was on the "cell overlap" between the upper and lower overturning cell. We highlight that this cell overlap is associated with the diabatic extension of the AMOC below the maximum depth of adiabatic upwelling in the Southern Ocean. The presence and magnitude of this diabatic extension critically depends on the magnitude of the diapycnal diffusivity, with strong diffusivity favoring a substantial diabatic extension and thus a large overlap. The overlap is further promoted by reducing the interhemispheric contrast in minimum surface buoyancy, which leads to a deepening of the upper cell in the Atlantic, as previously shown by Jansen and Nadeau (2016). All main results were validated using GCM simulations in an idealized two-basin configuration.

We also explored the role of ocean geometry in both the toy model and GCM. Results show that the globally integrated MOC depends to zeroth order on the length of the Southern Ocean channel (which determines the strength of the adiabatic upper cell) and the globally integrated basin area (which controls the diabatic extension), while being only weakly dependent on how that area is distributed over the basins. A zeroth-order understanding of the global MOC can thus be obtained using established single-basin theories, as long as the full length of the Southern Ocean and global ocean area are taken into account.

Our idealized approach necessarily implies that various physical mechanisms have been omitted or simplified in this study. Among these is the complex coupled interaction of the ocean with the atmosphere and sea ice, the nonlinearity of the equation of state, and the interplay between bathymetry and diapycnal mixing. However, the simplicity of our approach allows us to isolate key factors controlling the structure of the MOC and the exchange rate between the two cells. Our results, moreover, confirm that the toy model is a useful tool to understand the response of the MOC to various external parameters. The flexible structure of the model, which is freely available on GitHub, allows it to be readily extended to include more realistic boundary conditions, improved representations of diapycnal mixing, or any other parameterizations that may be of importance for future studies.

Acknowledgments. The toy model used for this study is available on GitHub at https://github.com/pymoc/PyMOC. The MITgcm is available at https://github.com/MITgcm/, and the specific configuration files used for the simulations in this study are available upon request from LPN. MFJ acknowledges support from NSF Award OCE-1846821. LPN acknowledges support from NSERC and FRQNT.

REFERENCES

Adkins, J. F., 2013: The role of deep ocean circulation in setting glacial climates. *Paleoceanography*, 28, 539–561, https://doi.org/ 10.1002/palo.20046.

Baker, J. A., A. J. Watson, and G. K. Vallis, 2020: Meridional overturning circulation in a multi-basin model. Part I: Dependence on southern ocean buoyancy forcing. J. Phys. Oceanogr., 50, 1159– 1178, https://doi.org/10.1175/JPO-D-19-0135.1.

Broecker, W. S., 1991: The great ocean conveyor. *Oceanography*, **4**, 79–89, https://doi.org/10.5670/oceanog.1991.07.

- Brovkin, V., A. Ganopolski, D. Archer, and S. Rahmstorf, 2007: Lowering of glacial atmospheric CO₂ in response to changes in oceanic circulation and marine biogeochemistry. *Paleoceanography*, 22, PA4202, https://doi.org/10.1029/ 2006PA001380.
- Burke, A., A. L. Stewart, J. F. Adkins, R. Ferrari, M. F. Jansen, and A. F. Thompson, 2015: The glacial mid-depth radiocarbon bulge and its implications for the overturning circulation. *Paleoceanography*, 30, 1021–1039, https://doi.org/10.1002/2015PA002778.
- Cessi, P., 2019: The global overturning circulation. Annu. Rev. Mar. Sci., 11, 249–270, https://doi.org/10.1146/annurev-marine-010318-095241.
- —, and C. S. Jones, 2017: Warm-route versus cold-route interbasin exchange in the meridional overturning circulation. *J. Phys. Oceanogr.*, 47, 1981–1997, https://doi.org/10.1175/JPO-D-16-0249.1.
- Curry, W. B., and D. W. Oppo, 2005: Glacial water mass geometry and the distribution of δ^{13} C of Σ CO₂ in the western Atlantic Ocean. *Paleoceanography*, **20**, PA1017, https://doi.org/10.1029/2004PA001021.
- Ferrari, R., M. F. Jansen, J. F. Adkins, A. Burke, A. L. Stewart, and A. F. Thompson, 2014: Antarctic sea ice control on ocean circulation in present and glacial climates. *Proc. Natl. Acad. Sci.* USA, 111, 8753–8758, https://doi.org/10.1073/pnas.1323922111.
- ——, L.-P. Nadeau, D. P. Marshall, L. C. Allison, and H. L. Johnson, 2017: A model of the ocean overturning circulation with two closed basins and a reentrant channel. *J. Phys. Oceanogr.*, 47, 2887–2906, https://doi.org/10.1175/JPO-D-16-0223.1.
- Gnanadesikan, A., 1999: A simple predictive model for the structure of the oceanic pycnocline. *Science*, 283, 2077–2079, https://doi.org/10.1126/science.283.5410.2077.
- Jansen, M. F., 2017: Glacial ocean circulation and stratification explained by reduced atmospheric temperature. *Proc. Natl. Acad. Sci. USA*, 114, 45–50, https://doi.org/10.1073/pnas.1610438113.
- —, and L.-P. Nadeau, 2016: The effect of Southern Ocean surface buoyancy loss on the deep ocean circulation and stratification. *J. Phys. Oceanogr.*, 46, 3455–3470, https://doi.org/10.1175/JPO-D-16-0084.1.
- ——, and ——, 2019: A toy model for the response of the residual overturning circulation to surface warming. *J. Phys. Oceanogr.*, **49**, 1249–1268, https://doi.org/10.1175/JPO-D-18-0187.1.
- Jones, C. S., and P. Cessi, 2016: Interbasin transport of the meridional overturning circulation. *J. Phys. Oceanogr.*, **46**, 1157–1169, https://doi.org/10.1175/JPO-D-15-0197.1.
- —, and R. P. Abernathey, 2019: Isopycnal mixing controls deep ocean ventilation. *Geophys. Res. Lett.*, 46, 13 144–13 151, https:// doi.org/10.1029/2019GL085208.
- Lumpkin, R., and K. Speer, 2007: Global ocean meridional overturning. J. Phys. Oceanogr., 37, 2550–2562, https://doi.org/ 10.1175/JPO3130.1.
- Marshall, D. P., and L. Zanna, 2014: A conceptual model of ocean heat uptake under climate change. *J. Climate*, **27**, 8444–8465, https://doi.org/10.1175/JCLI-D-13-00344.1.
- Marshall, J., and T. Radko, 2003: Residual-mean solutions for the Antarctic circumpolar current and its associated overturning circulation. J. Phys. Oceanogr., 33, 2341–2354, https://doi.org/ 10.1175/1520-0485(2003)033<2341:RSFTAC>2.0.CO;2.
- —, C. Hill, L. Perelman, and A. Adcroft, 1997: A finite-volume, incompressible navier stokes model for studies of the ocean on parallel computers. *J. Geophys. Res.*, **102**, 5753–5766, https://doi.org/10.1029/96JC02775.
- Marzocchi, A., and M. F. Jansen, 2017: Connecting Antarctic sea ice to deep-ocean circulation in modern and glacial climate simulations. *Geophys. Res. Lett.*, 44, 6286–6295, https:// doi.org/10.1002/2017GL073936.

- —, and —, 2019: Global cooling linked to increased glacial carbon storage via changes in Antarctic sea ice. *Nat. Geosci.*, 12, 1001–1005, https://doi.org/10.1038/s41561-019-0466-8.
- Nadeau, L.-P., R. Ferrari, and M. F. Jansen, 2019: Antarctic sea ice control on the depth of North Atlantic deep water. *J. Climate*, 32, 2537–2551, https://doi.org/10.1175/JCLI-D-18-0519.1.
- Newsom, E. R., and A. F. Thompson, 2018: Reassessing the role of the Indo-Pacific in the ocean's global overturning circulation. *Geophys. Res. Lett.*, **45**, 12 422–12 431, https://doi.org/10.1029/2018GL080350.
- Nikurashin, M., and G. Vallis, 2011: A theory of deep stratification and overturning circulation in the ocean. *J. Phys. Oceanogr.*, **41**, 485–502, https://doi.org/10.1175/2010JPO4529.1.
- —, and —, 2012: A theory of the interhemispheric meridional overturning circulation and associated stratification. J. Phys. Oceanogr., 42, 1652–1667, https://doi.org/10.1175/JPO-D-11-0189.1.
- Schmittner, A., J. Green, and S.-B. Wilmes, 2015: Glacial ocean overturning intensified by tidal mixing in a global circulation model. *Geophys. Res. Lett.*, 42, 4014–4022, https://doi.org/ 10.1002/2015GL063561.
- Shin, S.-I., Z. Liu, B. L. Otto-Bliesner, J. E. Kutzbach, and S. J. Vavrus, 2003: Southern Ocean sea-ice control of the glacial North Atlantic thermohaline circulation. *Geophys. Res. Lett.*, 30, 1096, https://doi.org/10.1029/2002GL015513.
- Sigman, D. M., and E. A. Boyle, 2000: Glacial/interglacial variations in atmospheric carbon dioxide. *Nature*, 407, 859–869, https://doi.org/10.1038/35038000.
- Stephens, B. B., and R. F. Keeling, 2000: The influence of Antarctic sea ice on glacial-interglacial CO₂ variations. *Nature*, **404**, 171–174, https://doi.org/10.1038/35004556.
- Sun, S., I. Eisenman, and A. L. Stewart, 2018: Does southern ocean surface forcing shape the global ocean overturning circulation? *Geophys. Res. Lett.*, 45, 2413–2423, https://doi.org/ 10.1002/2017GL076437.
- —, —, L. Zanna, and A. L. Stewart, 2020: Surface constraints on the depth of the Atlantic meridional overturning circulation: Southern Ocean versus North Atlantic. *J. Climate*, 33, 3125–3149, https://doi.org/10.1175/JCLI-D-19-0546.1.
- Talley, L. D., 2013: Closure of the global overturning circulation through the Indian, Pacific, and Southern Oceans: Schematics and transports. *Oceanography*, 26, 80–97, https://doi.org/10.5670/ oceanog.2013.07.
- Thompson, A. F., A. L. Stewart, and T. Bischoff, 2016: A multi-basin residual-mean model for the global overturning circulation. *J. Phys. Oceanogr.*, **46**, 2583–2604, https://doi.org/10.1175/JPO-D-15-0204.1.
- Toggweiler, J. R., and B. Samuels, 1998: On the ocean's large-scale circulation near the limit of no vertical mixing. *J. Phys. Oceanogr.*, **28**, 1832–1852, https://doi.org/10.1175/1520-0485(1998)028<1832: OTOSLS>2.0.CO;2.
- Watson, A. J., G. K. Vallis, and M. Nikurashin, 2015: Southern ocean buoyancy forcing of ocean ventilation and glacial atmospheric CO₂. Nat. Geosci., 8, 861–864, https://doi.org/10.1038/ngeo2538.
- Wolfe, C. L., and P. Cessi, 2009: Overturning circulation in an eddy-resolving model: The effect of the pole-to-pole temperature gradient. *J. Phys. Oceanogr.*, 39, 125–142, https://doi.org/ 10.1175/2008JPO3991.1.
- —, and —, 2011: The adiabatic pole-to-pole overturning circulation. J. Phys. Oceanogr., 41, 1795–1810, https://doi.org/10.1175/2011JPO4570.1.
- Wunsch, C., and R. Ferrari, 2004: Vertical mixing, energy, and the general circulation of the oceans. *Annu. Rev. Fluid Mech.*, 36, 281–314, https://doi.org/10.1146/annurev.fluid.36.050802.122121.